Hard carbon derived from coconut shells, walnut shells, and corn silk biomass waste exhibiting high capacity for Na-ion batteries

Cristina Nita[a,b,c], Biao Zhang[d], Joseph Dentzer[a,b], Camélia Matei Ghimbeu[a,b,e,*]

[a]*Université de Haute-Alsace, Institut de Science des Matériaux de Mulhouse (IS2M), CNRS UMR 7361, F-68100 Mulhouse, France*

[b]*Université de Strasbourg, F-67081 Strasbourg, France*

[c]*Center for Advanced Laser Technologies (CETAL), National Institute for Lasers, Plasma and Radiation Physics, Atomistilor 409 bis, RO-77125, Magurele, Romania*

[d] *Department of Applied Physics, The Hong Kong Polytechnic University, Kowloon, Hong Kong, China*

[e]*Réseau sur le Stockage Electrochimique de l'Energie (RS2E), CNRS FR3459, 33 Rue Saint Leu, 80039 Amiens Cedex, France*

*Corresponding author.

E-mail: camelia.ghimbeu@uha.fr

Tel: + 33 (0) 3 89 60 87 43

Abstract

In recent years, hard carbon materials have gained significant interest as anode materials for Na-ion batteries. Biomass waste is considered one of the most interesting, renewable, available, and cost-effective precursor to obtain hard carbon (HC); however, HC properties must be finely tuned to achieve performance comparable to those provided by Li-ion batteries. In this work, three biomass wastes (coconut shells, walnut shells, and corn silk) were evaluated as potential precursors for HC preparation involving a pyrolysis process and subsequent acid washing to remove the inorganic impurities. All obtained materials exhibited low and similar specific surface areas (< 10 $m^2 \cdot g^{-1}$), but they presented different structures and surface functionalities. The walnut shell HC possessed a lower amount of inorganic impurities and oxygen-based functional groups compared to the coconut shell and corn silk HCs, leading to higher initial coulombic efficiency (iCE). The structural organization was higher in the case of the walnut shell HC, while the corn silk HC revealed a heterogeneous structure combining both highly disordered carbon and localized graphitized domains. All HCs delivered high initial reversible capacities between 293 and 315 mAh g^{-1} at 50 mA g^{-1} current rate, which remained rather stable during long-term cycling. The best capacity (293 mAh g^{-1} after 100 charge/discharge cycles) and highest capacity retention (93%) was achieved in walnut HCs in half-cells, which could be associated with its higher sp^2 C content, better organized structure, and fewer impurities. An "adsorption-insertion" Na storage mechanism is suggested based on several techniques. The walnut HCs exhibited an attractive energy density of 279 Wh/kg when tested in full cells.

Keywords: Biomass; Pyrolysis; Hard carbon; Anode; Na-ion batteries; Energy storage

1. Introduction

In recent years, the increased development of industrial activities along with population growth around the world have triggered several environmental problems. The main energy resources are largely fossil fuels that produce greenhouse gases known to be responsible for the global temperature increase and climate change. Although renewable energy resources (e.g., sunlight, wind, tides) may present a green alternative, their current use is still very limited compared to fossil fuels, although, a gentle, increasing trend in their usage can be observed. In addition, such intermittent energy resources require efficient energy storage systems to store energy when available and to deliver when needed. For this purpose, Li-ion batteries (LIBs) are the most employed devices due to their low cost, high density energy, and broad application [1]. However, with the increased demand for batteries to accompany the energetic transition from fossil fuels to renewable resources, for implementation in electrical vehicles and other small devices, lithium availability is becoming a serious limitation. In fact, the available lithium resources are estimated to last for a maximum of 50 years; moreover, they are unequally localized worldwide [2]. Other battery components such as cobalt (Co) or copper (Cu)-based compounds have also become scarcer in nature. For these reasons, immense efforts have been made in recent years to find alternatives to Li-ion batteries.

Na-ion batteries have attracted great attention in the last five years due to the high availability of Na in seawater and the earth's crust, low price, and similar chemistry to LIBs. The possibility of using cheaper and lighter Al current collectors instead of Cu, for both the anode and cathode, is another advantage of such technology. On the other hand, Na is much larger and heavier than Li, leading to a lower energy density than LIBs. In addition, Na intercalation into graphite (the anode used for LIBs) is not favorable due to the weak interaction of Na into the graphite [3] and narrow graphite interlayer space (d_{002}); consequently, very low capacity was reported [4]. To overcome this inconvenience, other types of carbon materials have been evaluated for NIBs, such as porous carbons, graphene, doped carbon, and hard carbons (HCs).

Hard carbon, which possesses a disordered structure with large d_{002} space and defects, proved to be particularly efficient for Na insertion. HC is composed of a mixture of highly disordered carbon and pseudo-graphitized domains, which are arranged in a random fashion, and micropores that are located between these structures. The insertion of Na occurs in two stages as observed in a galvanostatic/charge discharge curve: a so-called sloping region at high

voltage (> 0.1 V) and a plateau region at low voltage (< 0.1 V). Although the precise attribution of the sloping and plateau regions is still a highly debated subject in the literature, the insertion of Na between the graphene layers, carbon pores, and defects is the main mechanism proposed [4-10].

Therefore, tuning the hard carbon structure, porosity, surface chemistry, and defects is of great interest in order to achieve performing anodes for NIBs. To this end, several studies have focused on the impact of precursor type and synthesis conditions (e.g., temperature, activation, doping) on carbon properties and significant differences were observed. Natural bio-polymers (cellulose, chitosan, sucrose, lignin) [11-14], polymers (phenolic resin, polyacrylonitrile, polyaniline) [15-17], and biomass and biomass waste (fruits shells and woods) [18, 19] were evaluated as precursors for HC preparation. In particular, biomass is the most studied category so far because of its availability, low price, and the possibility of contributing to the circular economy by transforming waste into value-added compounds.

Biomass wastes such as banana [20], mangosteen [21], argan [22], corn cob [23], wood [24], and many others [25-27] have been employed to obtain hard carbon via pyrolysis at high temperatures (usually > 1000 °C). These studies showed that for a given temperature, the properties of the obtained carbons are dependent on the precursor and its initial macromolecular and chemical structure. Moreover, the pyrolysis temperature also strongly affects the HCs properties. Generally, decreases in the specific surface area, graphitic interlayer space, functional groups, and defects are reported after increasing the temperature (1000–1600 °C) [7]. Regarding the electrochemical performance, a strong interdependence of several carbon properties may lead to improved performance, and a temperature range between 1300–1500 °C also appears to be favorable in ensuring a good compromise between the reversible/irreversible capacity and long-term cycle ability [28].

In this work, the impact of three biomass wastes (coconut shells, nutshells, and corn silk) on the derived hard carbon properties and performance in Na-ion batteries was evaluated. In particular, coconut shells are a very important source of waste in many tropical countries with a production of ~60 million metric tons/year [29]. It has a high calorific value and can be used to produce steam, energy-rich gases, bio-oil, and biochar [30]. It is highly used in industry and in the literature on the production of activated porous carbons. However, to date, there have been no reports regarding non-porous hard carbon for Na-ion batteries using this valuable and renewable resource. On the other hand, walnut and corn silk, although they are found in lower amounts in nature compared to coconut shells, are also important sources of carbon that can be

explored. These precursors present different macromolecular structures, i.e., coconut shells have a well-balanced composition between lignin, cellulose, and hemicellulose [31]; walnut shells have a predominant composition of cellulose (~50%) and similar amounts of hemicellulose and lignin [32]; and corn silk contains mainly cellulose/hemicellulose and a low amount of lignin in their structure. In addition, they contain different amounts of ash produced from the inherent inorganic matter in their structure. Their different organic and inorganic compositions lead to different carbon features and good performance in Na-ion batteries, i.e., a capacity between 293 and 315 mAh g^{-1} at 50 mA g^{-1} with good retention (87–93%) after 100 cycles. An "adsorption-intercalation" mechanism is suggested herein based on several techniques. The potential of these materials in full cells has also been demonstrated.

2. Experimental

2.1 Hard carbon synthesis

Three raw biomass (coconut shells, walnut shells, and corn silk) were ground in small parts and thermally annealed under an inert atmosphere (Ar) up to 1300 °C for 1 h at a heating rate of 5 °C min^{-1}. The obtained hard carbon materials were washed with an aqueous solution of HCl (18 vol%) at room temperature for a few hours, filtered, rinsed abundantly with distilled water, and dried under air at 80 °C for one night. The as-synthesized hard carbons were denoted as HC-W (W-from walnut), HC-C (C- from coconut), and HC-S (S-from silk). A schematic illustration of the synthesis process is provided in Fig. 1.

2.2 Physicochemical characterization

The decomposition of biomass precursors was followed with thermogravimetric analysis (TGA) using a TGA 851 (Mettler-Toledo) instrument. The samples were heated under a nitrogen atmosphere (flow rate 100 mL min^{-1}) at a heating rate of 5 °C min^{-1} up to 900 °C, and the mass loss was recorded. The morphology of the hard carbon materials was investigated using an FEI Quanta 400 scanning electron microscope. An energy dispersive analyzer (EDX) connected to the SEM set-up was used to determine the chemical composition of the hard carbon materials. Three spectra were acquired in different places to be representative of the entire material and the average values were calculated and reported. The hard carbon structure

was evaluated using X-ray diffraction (XRD) with a Bruker D8 Advanced diffractometer that had a Bragg-Brentano θ-θ geometry. This instrument was equipped with a LynxEye XE-T high-resolution energy dispersive 1-D detector (Cu K$\alpha_{1,2}$). The interlayer distance (d_{002}) was calculated using the (002) graphite diffraction peak and Bragg equation (1):

$$d_{002} = \frac{\lambda}{2\sin\theta} \qquad (1)$$

where λ is the X-ray wavelength (1.5406 Å) and θ is the scattering angle corresponding to the peak position.

The crystallite size along the c-axis, *L*c (staked plane height) and the size of the layer planes (staked plane width) *L*a were calculated from the full width at half maximum (FWHM) of the (002) and (100) diffraction peaks, respectively, using the Scherrer formula (2) [33]:

$$L = \frac{K\lambda}{B\cos\theta} \quad (2)$$

where K is a shape factor and has a value of 0.9 and 1.84 for *L*c and *L*a, respectively, and B is the peak full width at half maximum (in radians).

The local structure of the hard carbon materials was characterized through Raman spectroscopy using a LabRAM BX40 (Horiba Jobin-Yvon) spectrometer equipped with a He-Ne excitation source (532 nm wavelength). Several spectra (9) were acquired, and the average spectrum was used to ensure good representation of the material structure. Raman analyses on hard carbon electrodes (pristine and fully discharged) were performed using a Witec-Confocal Raman system with a laser wavelength of 532 nm.

The textural properties of hard carbons were assessed with the help of a Micromeritics ASAP 2420 instrument using N_2 as the gas probe (77 K) and a Micromeritics ASAP 2020 using CO_2 gas (273 K). The materials were outgassed for 12 h at 300 °C under vacuum to remove physisorbed molecules. The Brunauer-Emmett-Teller (BET) specific surface area (SSA) was calculated in the relative pressure ranges of 0.05–0.3 and 0.01–0.03 for N_2 and CO_2, respectively. The pore size distribution (PSD) was determined from N_2/CO_2 adsorption branch isotherms *via* the non-local density functional theory (NLDFT) and standard slit pore model for carbon materials, using the SAIEUS 2.02 software (Micromeritics). The surface chemical composition was determined through X-ray photoelectron spectroscopy (XPS) using a VG SCIENTA SES-2002 spectrometer equipped with a concentric hemispherical analyzer. The incident radiation used was generated by a monochromatic Al *K*α X-ray source (1486.6 eV) operating at 420 W (14 kV; 30 mA).

The active surface area (ASA) was determined through temperature-programmed desorption coupled with mass spectrometry (TPD-MS) using a custom build setup. First, the carbon surface was cleaned *via* heating under vacuum up to 950 °C in order to remove the oxygen functional groups, and then it was subjected to di-oxygen chemisorption (66.5 MPa) at 300 °C for 10 h. After cooling, the sample was heated under vacuum (up to 950 °C) and the formed species were decomposed by releasing H_2, H_2O, CO, and CO_2, which were continuously monitored using a mass spectrometer. The integration of CO and CO_2 desorption curves allowed the assessment of the quantity and ASA, taking into consideration that one carbon edge site is able to chemisorb an oxygen atom has a surface of 0.083 nm^2 [7].

2.3. Electrochemical characterization

To obtain the carbon electrodes, a slurry was prepared by mixing the hard carbon active material, a conductive carbon additive (Super P), and polyvinylidene fluoride (PVDF) binder in a weight ratio of 80:10:10 in N-methyl-2-pyrrolidone (NMP) solvent. The resulting mixture was coated on a copper foil and spherical electrodes were cut to a diameter of 12 mm, followed by a drying step in an oven. Prior to transferring the electrodes into a glovebox, vacuum drying was performed in a Buchi glass oven. The electrochemical tests were conducted in a half-cell configuration using coin cells (CR2032), Na metal as a counter electrode, glass fiber separator (Whatman, GF/D), and 1M $NaPF_6$ in diglyme as the electrolyte. The half-cells were charged/discharged on a Land BT2000 battery test system between 0 and 3 V at 25 mA g^{-1} for three cycles, increased to a constant specific current of 50 mA g^{-1} for long-term cycles. Cyclic voltammetry was performed by varying the scan rate from 0.1 to 1.0 mV s^{-1}. Full-cell tests were assembled using $Na_3V_2(PO_4)_2F_3$ (NVPF) as the cathode and HC-W hard carbon as the anode. The same electrolyte (1 M $NaPF_6$ in diglyme) was used, and the current density was approximately 10 mA g^{-1}. The specific capacity was calculated based on the mass of the cathode active material (6 mg).

3. Results and discussion

3.1 Physicochemical properties

The thermal decomposition behavior of the biomass materials is presented in Fig. 1 as weight percent loss (TGA curve) and its corresponding first derivative (DTG curve). Three main regions of mass loss were observed for all precursors. Below 120 °C, a small peak corresponding to the release of inherent water is observed, which represents approximately 5 wt% mass loss for all biomasses. Between 150 °C and 400 °C, a large mass weight loss occurs

(54–60 wt%), which is indicated by well-defined peaks in the DTG curves. This region is associated with the devolatilization of the biomass, and therefore, the active pyrolysis zone. The main lignocellulosic biomass constituents, i.e., hemicellulose, cellulose, and lignin, are decomposed in this region at temperatures of 200–280 °C, 260–350 °C, and 280–500 °C, respectively [34, 35]. In the case of walnut shells, one intense peak of decomposition is observed at approximately 355 °C with a small contribution at 290 °C, which is an indication of predominant cellulose decomposition and, to a lesser extent, hemicellulose [34]. Corn silk precursor also exhibits a main decomposition peak, but the temperature is much lower, i.e., 309 °C, compared to walnut shells (355 °C), suggesting a composition that is rather richer in hemicellulose. In general, corn silk shows a lower thermal stability-the degradation step is initiated at a lower temperature (~150 °C) than the other precursors (190 °C). For coconut shells, two peaks are visible at 274 and 344 °C, suggesting a well-balanced hemicellulose and cellulose content in the precursor, in agreement with previous works [35, 36]. At temperatures higher than 400 °C, a slow decomposition was observed, accounting for ~10 to 15 wt% mass loss, which can be associated with the decomposition of lignin, removal of some oxygenated functional groups, and carbon structure reorganization. The final residue content at 900 °C is ~25 wt% for coconut shells and corn silk and slightly lower for walnut shells (20 wt%). The differences in the observed residues are related to the biomass macromolecular composition, i.e., a higher lignin content corresponds to a higher residue amount, if one considers the higher lignin carbon yield (~40 wt%) [13] compared to cellulose (~10 wt%) [37]. Moreover, the values of the carbon yield are comparable to those of other biomass precursors used for hard carbon preparation, i.e., waste cork (20 wt%) [38], rice husk (24 wt%) [39] and corn cobs (21 wt%) [40].

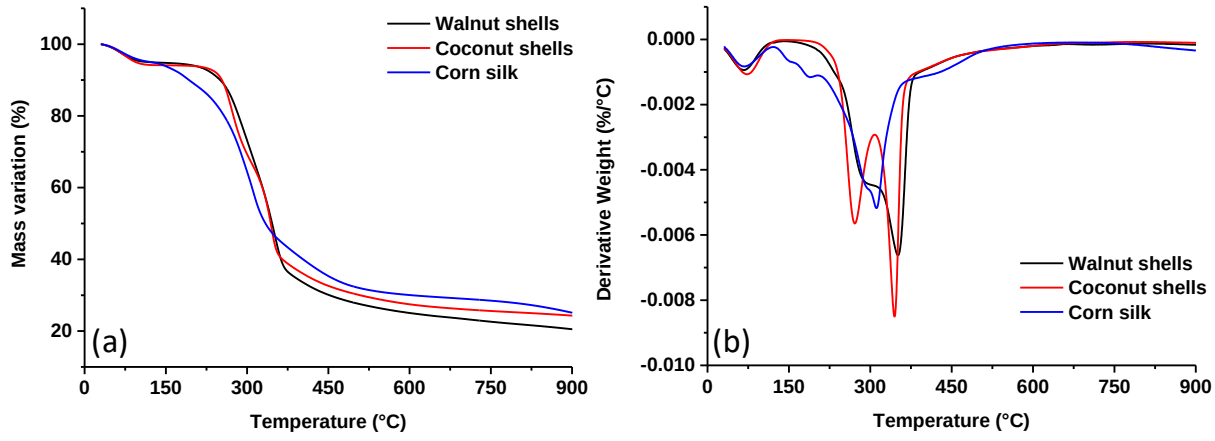

Fig. 1. *TGA (a) and the corresponding derivative DTG curves (b) of the three biomass materials.*

The carbon morphology studied using SEM revealed dense particles with pallet-like aspect and sizes between 5 and 20 µm in HC-W (Fig. 2a). For the HC-C material (Fig. 2b), the particle size was found to be much larger, sometimes exceeding 100 µm, with a surface showing spherical macropores (~ 2 µm). In contrast to these two materials, HC-S exhibited a fibrous structure with lengths of several hundred micrometers and diameters of 50–100 µm (*inset* of Fig. 2c). A closer inspection of the fiber (Fig. 2c) revealed that each fiber consists of several thinner fibers (diameter < 5 µm).

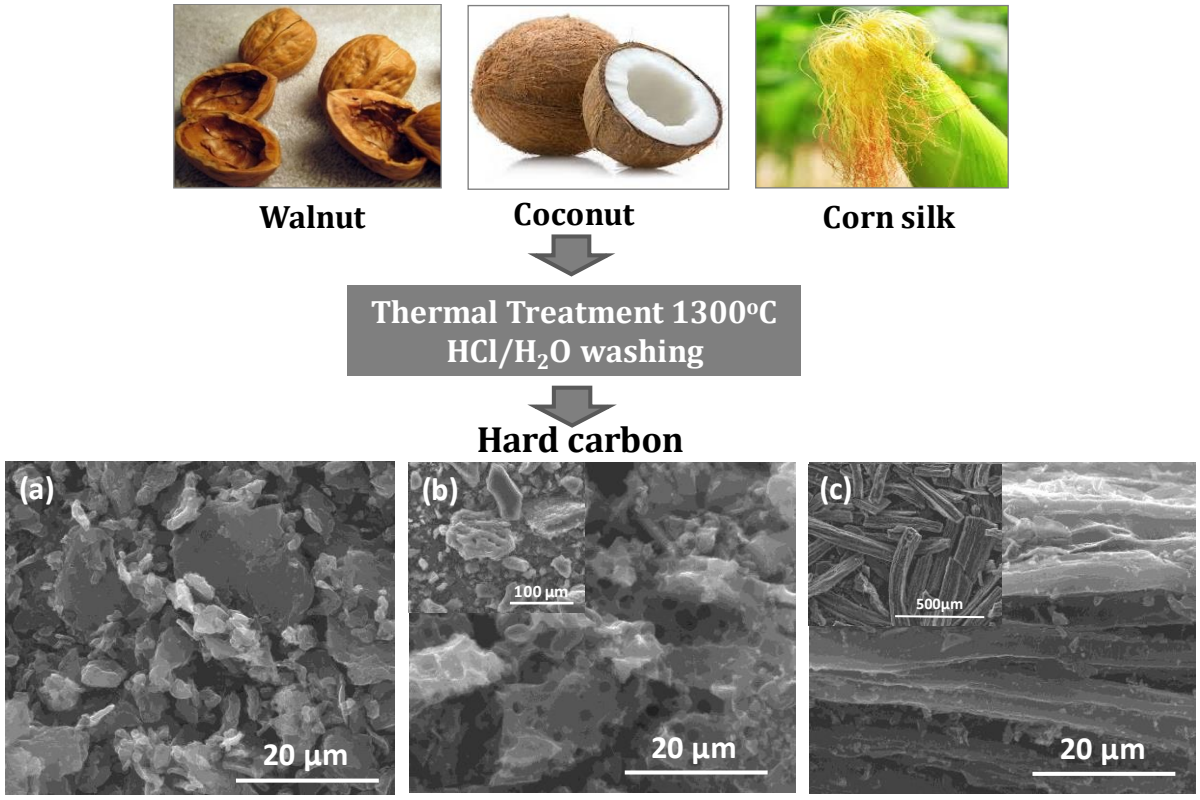

Fig. 2. *(top) Schema of hard carbon synthesis pathway of the three biomass materials and (bottom) their corresponding SEM images (a) HC-W, (b) HC-C and (c) HC-S.*

The chemical composition of the hard carbon materials was assessed using EDX analysis, and the average values of the chemical elements constituting the materials are reported in Table 1. The major component is C, which was found to be 95.02 at%, 93.51 at%, and 92.83 at%, of HC-W, HC-C, and HC-S, respectively. Oxygen was also detected, with a lower content in HC-W (4.66 at%) as compared to HC-S and HC-C (5.15 at% and 6.26 at%). The amount of oxygen comes partly from the carbon matrix (oxygen functionalities) and partly from inorganic impurities such as K, Ca, and Si, which were detected. The inorganic quantity, however, is less than 0.5 at% for HC-W and HC-C, while in the case of HC-S, the quantity is almost three times

higher due to the significant contribution of Si, which cannot be dissolved through HCl treatment. This later material also contains P (0.5 at%) and some traces of Cl in the structure.

Table 1. *Chemical composition of hard carbon materials determined using EDX.*

Material	C (at%)	O (at%)	K (at%)	Ca (at%)	Si (at%)	P (at%)	Cl (at%)
HC-W	95.02	4.66	0.22	0.26	-	-	-
HC-C	93.51	6.26	0.18	-	0.13	-	-
HC-S	92.83	5.15	0.41	0.13	0.85	0.52	0.17

The structure of hard carbon materials was first determined using XRD (Fig. 3a), which offers overall information about the graphitization degree, interlayer graphitic space, and their arrangement. For all materials, three main peaks are observed at approximately 23°, 44°, and 79° 2θ, corresponding to the (002), (100), and (110) reflection planes of graphite. As noticed, the peaks are broad, indicating disordered-like carbons with a low degree of graphitization. For HC-S, several, minute supplementary peaks are seen at 35°, 60°, and 72°, which could be assigned to SiC (PDF 29-1129). Another peak is observed at 31° and its position corresponds to K_2CO_3 (PDF 70-0292) or KO_2 (77-0211); however, precise identification could not be obtained due to the absence of supplementary diffraction peaks. These impurities originate from the biomass and could not be removed through HCl washing treatment. For the other materials, no crystalline impurities were observed.

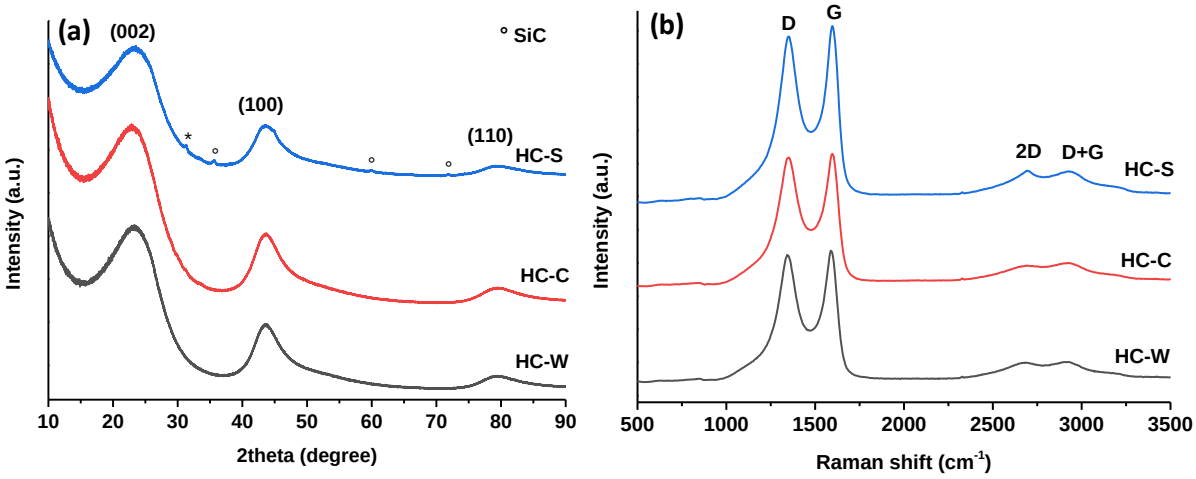

Fig. 3. *(a) XRD patterns and (b) Raman spectra of hard carbons derived from the different biomass materials: HC-W, HC-C, and HC-S.*

The interlayer space (d_{002}) was calculated and the obtained values were 3.70 Å, 3.75 Å, and 3.68 Å (Table 2) for HC-W, HC-C, and HC-S, respectively. HC-C has, therefore, the highest interlayer space and disordered degree. As the pyrolysis temperature was the same, the observed different d_{002} values were most probably induced by the precursor initial macromolecular and chemical structures [24]. However, for all materials, these values are larger than the d_{002} of graphite (3.4 Å), in agreement with other hard carbons prepared from different precursors at the same temperature range [9, 41]. It is worth mentioning that d_{002} is large enough to allow Na insertion into the carbon structure, considering the work of Cao *et al.* [6] which predicted using theoretical calculations that d_{002} must be at least 3.70 Å for the favorable insertion of Na into hard carbon. The graphene staked height, Lc, was found to be rather similar among the HCs (10 Å), suggesting that approximately 2–3 layers of graphene were stacked together. The graphene lateral size, La, exhibited values between 33 and 34 Å (Table 2).

Table 2. *Hard carbon properties including: d_{002}, Lc, and La determined using XRD, I_D/I_G deduced using Raman spectroscopy, SSA N_2 and SSA CO_2 obtained from gas adsorption, C and O amounts assessed using XPS and ASA obtained TPD-MS*.*

Material	d_{002} (Å)	*L*c (Å)	*L*a (Å)	I_D/I_G	SSA N_2 ($m^2\ g^{-1}$)	SSA CO_2 ($m^2\ g^{-1}$)	C (at%)	O (at%)	ASA ($m^2\ g^{-1}$)
HC-W	3.70	10	34	1.82	6	12	96.4	3.4	9
HC-C	3.75	10	33	1.86	7	15	89.5	8.5	6
HC-S	3.68	10	33	1.78	10	23	90.2	6.8	11

*d_{002}, interlayer space; *L*c, crystallite size; *L*a, crystallite length; SSA, specific surface area; ASA, active surface area.

Further insights into the carbon local structure were provided using Raman spectroscopy (Fig. 3b). Two intense peaks are observed at ~1350 and ~1590 cm^{-1}, which correspond to the D and G bands, respectively. The D band originates from the disordered A1g breathing mode of the polyhexagonal carbon structures, whereas the G band corresponds to the in-plane C-C stretching vibration of sp^2-hybridized graphitic carbon atoms (E2g mode) of the six-membered aromatic ring. The report I_D/I_G is often used to characterize the disordered degree in carbon

materials and the obtained values herein are 1.82 for HC-W, 1.86 for HC-C, and 1.78 for HC-S. The HC-C has the highest value, indicating the highest degree of disorder, in good agreement with the XRD results. For HC-S, the I_D/I_G values were the smallest, indicating a slightly more structurally organized material than HC-W; this can be also sustained by the more intense second-order Raman peaks (2D) ~2696 cm^{-1}. In the case of HC-S, some spectra revealed a highly intense 2D peak; however, it is worth noting that 9 spectra were acquired and only the averaged one is presented. Based on these spectra, it can be affirmed that the HC-S material possesses both disordered and more graphitized regions.

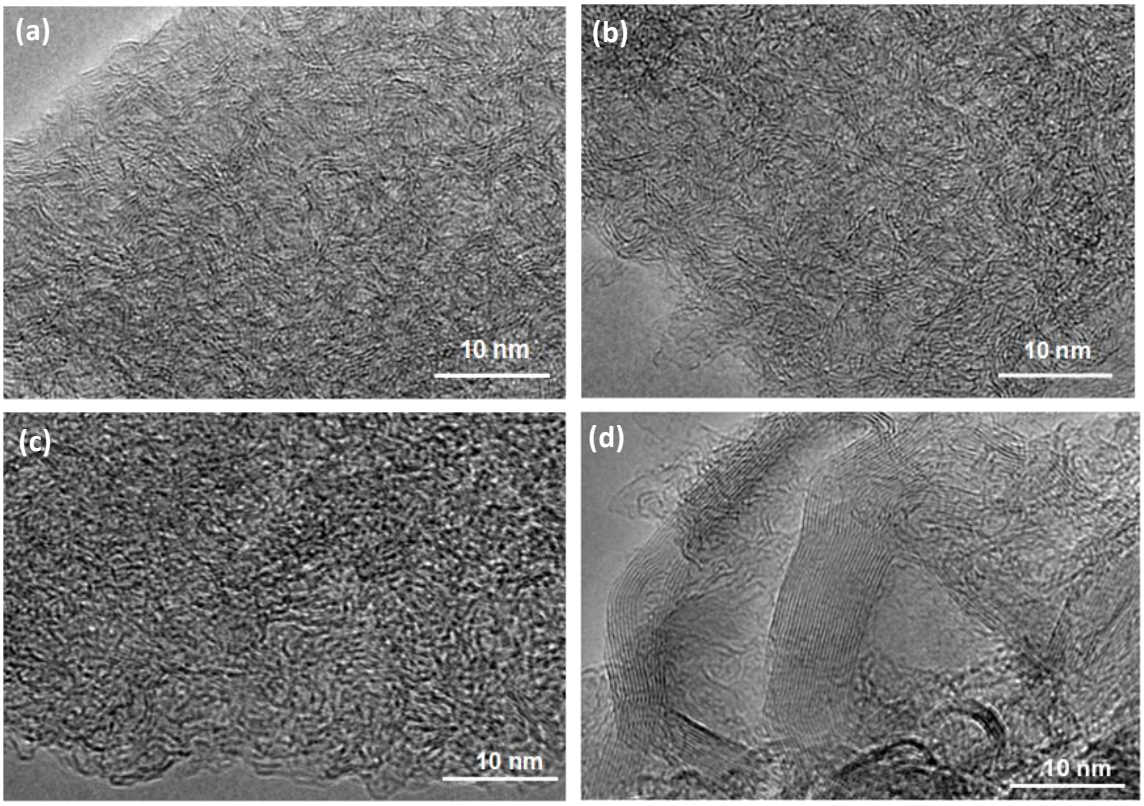

Fig. 4. *HRTEM images of hard carbons derived from different biomass materials (a) HC-W, (b) HC-C, and (c,d) HC-S.*

The high-resolution transmission electron microscopy (HRTEM) images (Fig. 4b,c) are consistent with the Raman analysis results. Rather disordered carbon structure with randomly oriented graphene sheets, with very little stacking can be seen (Fig. 4c), whereas other zones in the material (Fig. 4d) present large graphitic sheets of several tenths of nm, which are stacked in 10 to 20 graphene layers. This graphitization can be a result of carbon interaction with metallic impurities (Si, K) at high temperatures. Such metals are known to catalyze carbon and convert them into graphitic structures [42]. For HC-W and HC-C materials, the local structure

(Fig. 4a, b) is more homogeneous than in the previous case. It can be distinguished from a mixture of disordered like areas and small stacked graphene sheets resembling the “house of cards” model proposed by Dahn *et al.* [43]. Between these ordered and disordered carbon regions, voids are created, known as closed pores.

XPS was employed to obtain a deeper understanding of the surface chemistry of the prepared carbons (Fig. 5). Compared to EDX analysis, which provides an evaluation of the chemical composition in the bulk sample, XPS provides complementary insights regarding the nature of functional groups and the chemical bonds found in the extreme surface of the material (~10 nm depth). The wide XPS profiles (Fig. 5a) revealed the presence of an intense peak C 1*s* and several other smaller peaks corresponding to O 1*s*, K 2*s*, Si 2*p*, and Cl 2*p*. The amount of carbon is 96.4 at% for HC-W, 89.5 at% for HC-C, and 90.2 at% for HC-S (Table 2). Therefore, HC-W has the highest amount of carbon in the structure, which can not only ensure a larger carbon host for Na insertion but also better electronic conductivity.

The amount of oxygen was the highest for HC-C (8.5 at%), followed by HC-S (6.8 at%) and HC-W (3.4 at%), a trend evolution similar to that observed using EDX (Table 1). A certain quantity of oxygen may be desirable to improve the wettability of the materials with the electrolyte. However, larger amounts may induce electrolyte decomposition with the formation of a solid electrolyte interphase (SEI) and consequently a high irreversible capacity in the first charge/discharge cycles [44, 45].

Among the carbons, HC-W showed the smallest amount of impurities (0.23% Cl), while HC-S had the highest amount (1.23 at% K, 1.24 at% of Si, and 0.66 at% Cl) and HC-C had intermediate amounts (1.69 at% K and 0.31 at% Na). The metallic impurities originate from the initial composition of the biomass, while Cl presence resulted from the washing step performed to remove a large part of these impurities. A closer look at the C 1*s* peak (284 eV, Fig. 5b) shows that the peak is much thinner for HC-W than for the other two carbons. The deconvolution of the C 1*s* peaks (Fig. 5c, d) evidences a strong contribution of C sp^2 to the C 1*s* peak for all materials, with the largest amount being for HC-W, 85.8 at%, followed by HC-S, 76.8 at% and HC-C, 73.4 at% (Fig. 5d). The HC-W does not present C sp^3, unlike HC-C and HC-S, where contribution below 5 at% is observed, suggesting more disordered structures. Several oxygen functional groups were detected at 286.0 eV, 287.2 eV, and 288.4 eV corresponding to ether (C-OR), carbonyl (C=O), and carboxyl (COOR) groups, respectively.

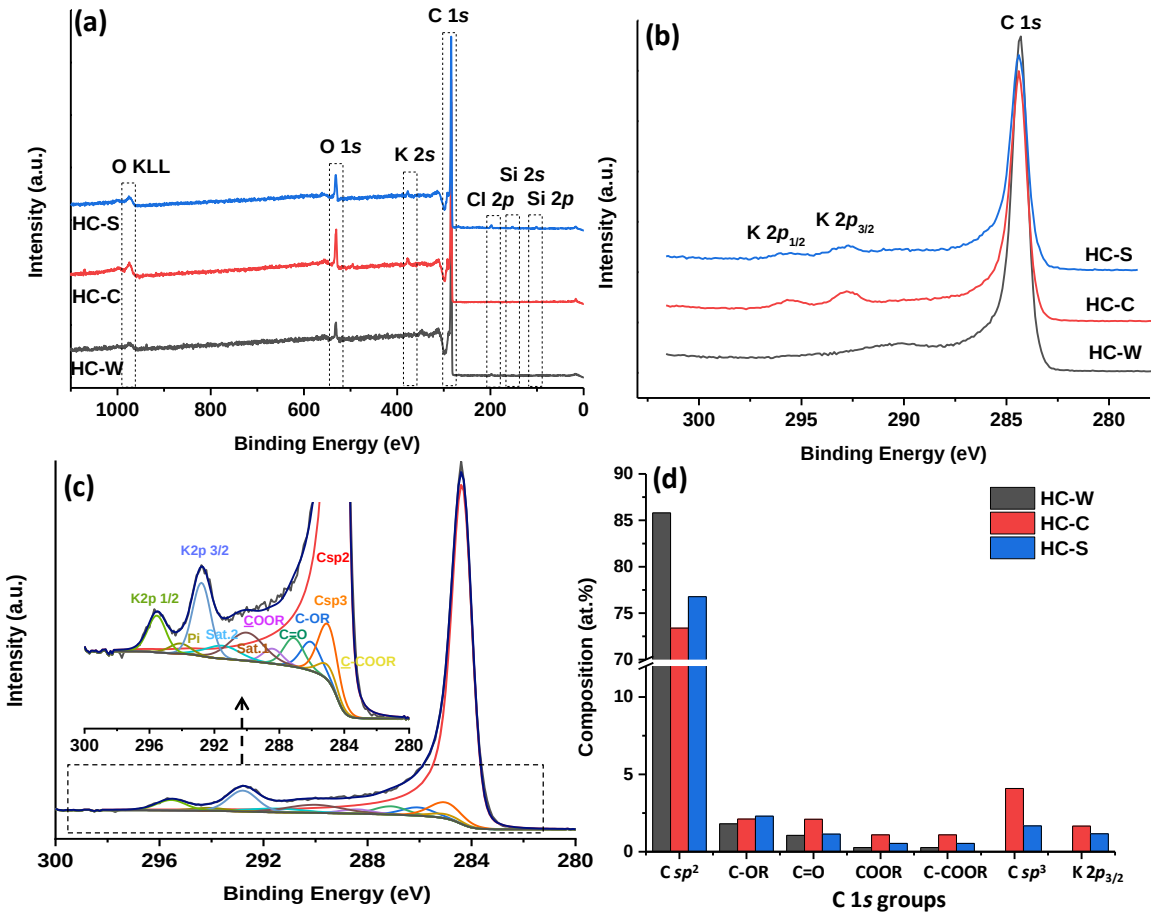

Fig. 5. *(a) Wide XPS profiles of HCs, (b) high resolution C 1s XPS peaks of HCs, (c) deconvoluted high resolution C 1s peak for HC-C, and (d) repartition of functional groups based on the deconvolution of C 1s peaks of each HC.*

More insights into the carbon structure and defects were obtained using the TPD-MS technique. After cleaning the carbon surface *via* vacuum heating (to remove naturally formed functional groups), the carbon was subjected to oxygen chemisorption to allow the interaction of active sites with oxygen and the formation of new oxygen-based functional groups. The desorption profiles of the gases from the decomposition of functional groups formed after oxygen chemisorption are shown in Fig. 6. For HC-W and HC-S materials, an intense CO peak at high temperatures between 600 and 950 °C was observed, whereas for HC-C, the CO peak was less intense. The release of CO in this temperature range is associated with the decomposition of phenol, ether, and quinone groups [7]. For CO_2 release, a much smaller peak was observed, indicating lower amounts of acidic oxygen-containing groups. For HC-W (Fig. 6a), the CO_2 peak is broad and found between 300 and 700 °C, suggesting the formation of carboxyl and anhydride groups after oxygen chemisorption. The presence of the latter groups is sustained by

the concomitant release of CO_2 and CO in the higher temperature range. In the case of HC-S (Fig. 6b), the CO_2 peaks are more visible at lower temperatures, i.e., 200 °C and 400 °C, with less contribution at 600 °C, while for HC-C (Fig. 6c), the peak at 400 °C became the predominant one. Therefore, for HC-S and HC-C, more carboxylic groups are evolved and their *in-situ* reactions during heating leads to anhydride and water release.

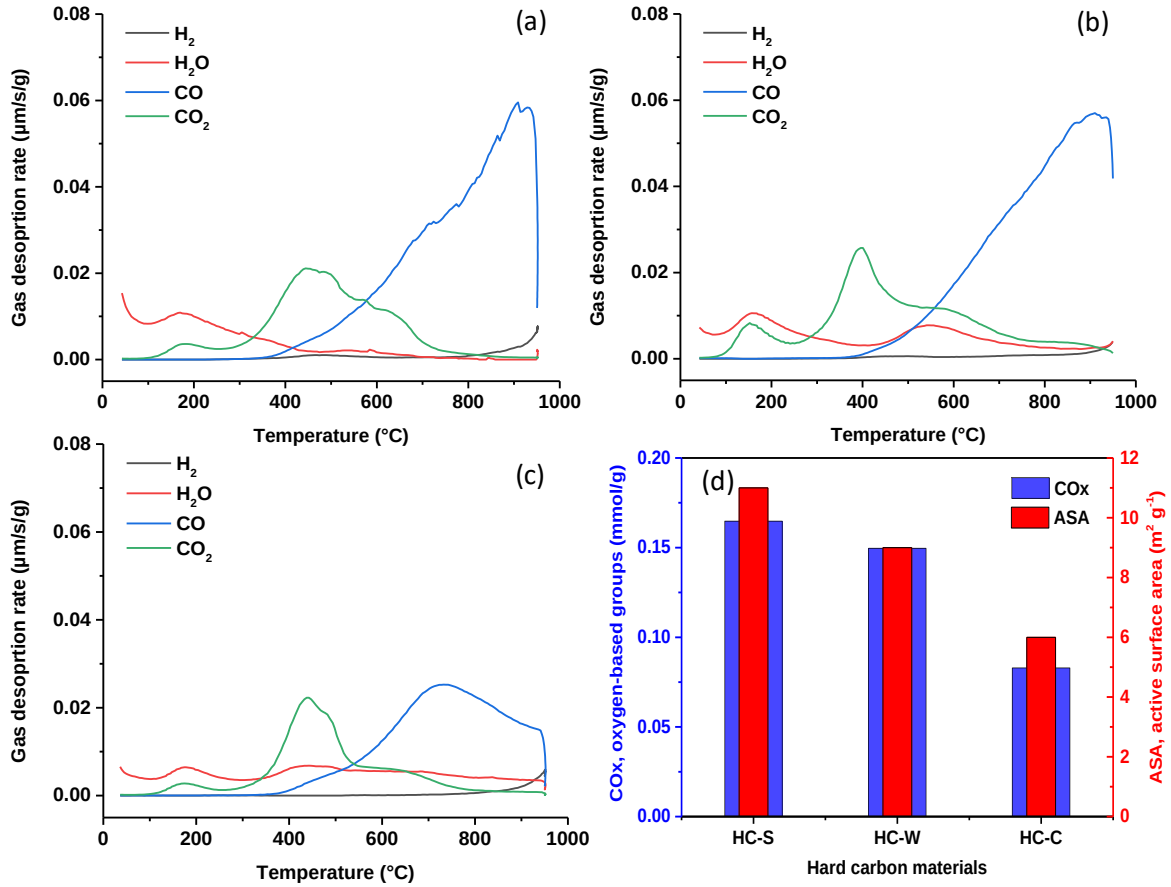

Fig. 6. *TPD-MS desorption profiles of (a) HC-W, (b) HC-S, and (c) HC-C after vacuum cleaning and oxygen chemisorption along with (d) the amount of oxygen-based CO_x (CO + CO_2) functional groups released and the active surface area, ASA.*

The difference in the oxygen-based groups observed between the materials (Fig. 6d) can be related to their structural organization and the presence of defects. The active sites, containing edge defects (e.g., stacking faults, dislocations) are quantified in terms of the active surface area (ASA), and the values found were the highest for HC-S (11 m^2 g^{-1}), followed by HC-W (9 m^2 g^{-1}) and HC-C (6 m^2 g^{-1}). Although the ASA values for hard carbon obtained from biomass have not yet been reported, the obtained values herein are in the same range as other hard carbons prepared from biopolymers at similar pyrolysis temperatures. For instance, hard

carbons derived from cellulose, lignin, or chitin showed ASA values of 7–12 m^2 g^{-1} [7], 9–12 m^2 g^{-1} [13] and 11 m^2 g^{-1} [12], respectively.

The hard carbon textural properties were evaluated using nitrogen adsorption/desorption isotherms and CO_2 adsorption isotherms (Fig. 7). For HC-W and HC-S, type IV nitrogen isotherms were observed, characterized by an increase in the adsorbed nitrogen volume at low relative pressures (P/P_0 < 0.1), followed by a hysteresis loop between 0.4 and 1.0 P/P_0. Such an isotherm is specific for materials containing both micro- and mesopores (Fig. 7a). However, the nitrogen adsorbed volumes are rather low and translate into a low specific BET surface area (6 m^2 g^{-1} for HC-W and 10 m^2 g^{-1} for HC-S). In the case of HC-C, a type I isotherm was observed with a low volume of nitrogen adsorbed, indicating the presence of only micropores (< 2 nm) and small specific surface area (7 m^2 g^{-1}, Table 2).

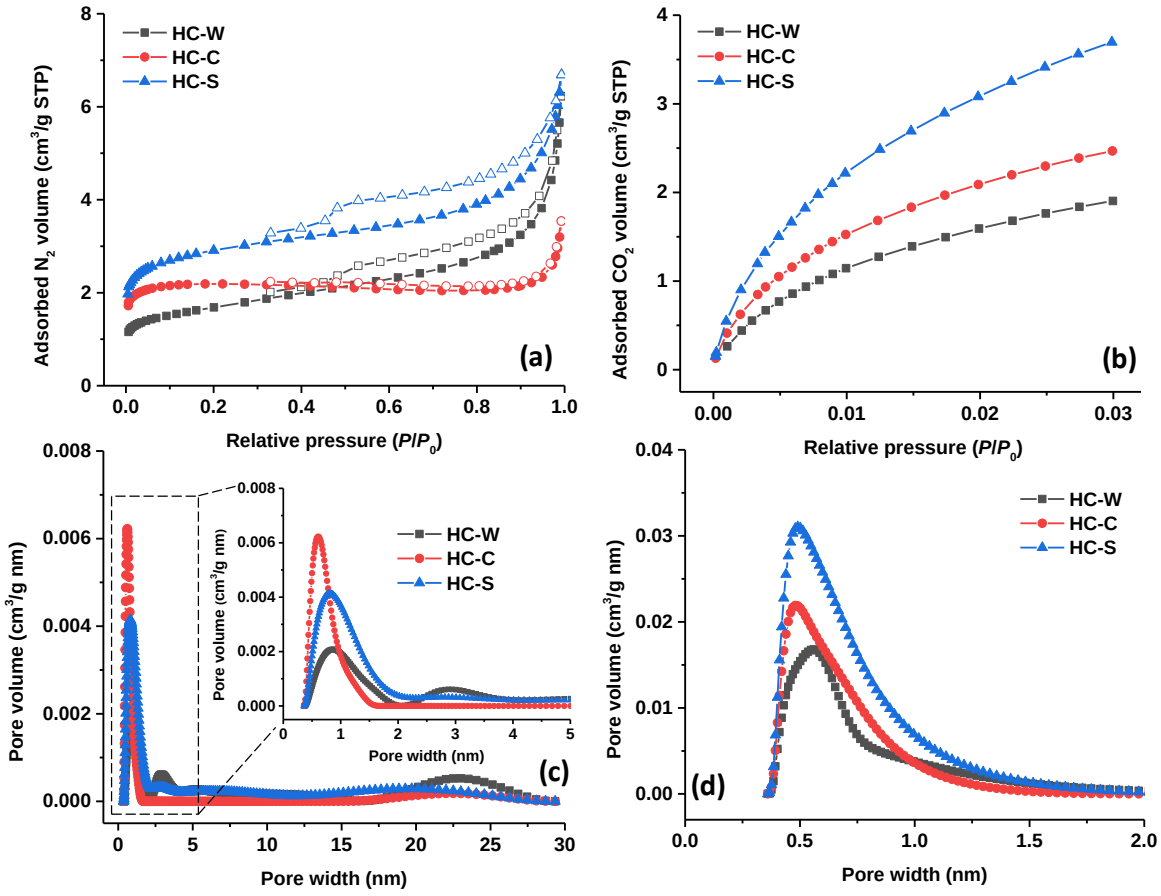

Fig. 7. *(a) Nitrogen adsorption/desorption isotherms and (b) CO_2 adsorption isotherms of hard carbons derived from different biomass materials and their corresponding 2D-NLDFT pore size distribution (c) N_2 and (d) CO_2, where full symbols denote adsorption and open symbols denote desorption.*

These results show that although different precursors were used, a low specific surface area could be achieved. This may be a consequence of the high annealing temperature used herein (1300 °C) which favors the pore closure phenomena based on the "falling card" model described by Dahn *et al.* [43]. For instance, walnut shells reported by Wahid *et al.* [46] exhibited a specific surface area of 120 m^2 g^{-1} at 800 °C, which progressively decreased to 59 m^2 g^{-1} and 19 m^2 g^{-1} at 1000 and 1200 °C, respectively. Similar results were observed when cellulose precursor was used, with a decrease in the SSA from 84 m^2 g^{-1} to 5 m^2 g^{-1} upon heating from 1000 °C to 1400 °C [7], or when using other precursors [47].

As demonstrated previously [7], CO_2 adsorption allows the detection of narrow pores (ultra-micropores < 0.7 nm) due to its better diffusion. The CO_2 adsorption isotherms also show low CO_2 adsorption volumes (Fig. 7b) and low specific surface areas (12, 15, and 23 m^2 g^{-1} for HC-W, HC-C, and HC-S, respectively). The low surface areas of the materials may be beneficial in reducing the side reactions of the carbon surface with the electrolyte to limit the SEI layer formation, and consequently to reduce the irreversible capacity in the first charge/discharge cycle [7].

The nitrogen pore size distribution (Fig. 7c) revealed a maximum contribution of approximately 1 nm for all material pore sizes. Some larger pores (20–25 nm) are seen in the HC-W material. In addition, ultra-micropores centered on 0.5–0.6 nm were detected in the CO_2 pore size distribution (Fig. 7d).

3.2 Electrochemical performance

Hard carbon performances for Na-storage were first assessed in half-cells (Fig. 8). For all materials, very high initial discharge capacities were recorded with 479, 463, and 504 mAh g^{-1} for HC-W, HC-C, and HC-S, respectively (Table 3). However, after charging, smaller capacities were recovered, i.e., 315, 294, and 314 mAh g^{-1}, leading to initial coulombic efficiencies of 66, 63, and 62% for HC-W, HC-C, and HC-S, respectively. This loss in capacity during the first discharge/charge curves is mainly associated with the creation of a solid electrolyte interphase (SEI) due to the interaction of the carbon surface with the electrolyte, leading to electrolyte decomposition and irreversible ion trapping in the carbon matrix. One key parameter that is often presented as critical for such undesirable reactions is the specific surface area [37]. It is worth noting that in the case of the present carbons, the BET SSA is small for all materials (below 10 m^2 g^{-1}, Table 1); therefore, this can only explain the observed results to a

small extent. Another important factor that may contribute to irreversible reactions can be the carbon functional groups and defects. In our previous work [7], a linear increase in Cirrev was observed with an increase in the number of oxygen-based functional groups and defects. Particularly, in the case of HC-C and HC-S, the oxygen group amount is higher than that in HC-W (Table 2), and the defect amounts (ASA) are also higher in HC-W and HC-S. Inorganic impurities (e.g., Si, K, Ca) were also identified as detrimental to the irreversible/reversible capacity and long-term cycle ability [12, 13, 48]. To recall, HC-W had the lowest amount of impurities and oxygen in the structure; therefore, this may explain the slightly better coulombic efficiency for this material. In addition, factors related to the electrolyte and Na-counter electrode quality (e.g., presence of water trace, oxide layer) can also contribute to undesired reactions [49].

In the 2nd cycle, the recorded reversible capacities were 314, 292, and 313 mAh g^{-1} for HC-W, HC-C, and HC-S, respectively, which are high values compared to other recent studies [9]. The coulombic efficiency greatly improved and reached approximately 95% in the 2nd cycle for all materials.

Table 3. *Electrochemical performance of hard carbon materials including 1st discharge and charge capacities (1st $C_{disch.}$ and 1st $C_{charg.}$), initial columbic efficiency (iCE), reversible charge capacity in the second and after the 100th cycles (2nd C_{charg} and 100th $C_{charg.}$) and the columbic efficiency after 100 cycles (100th CE).*

Material	1st $C_{disch.}$ (mAh g^{-1})	1st $C_{charg.}$ (mAh g^{-1})	iCE (%)	2nd $C_{charg.}$ (mAh g^{-1})	100th $C_{charg.}$ (mAh g^{-1})	100th CE (%)
HC-W	479	315	66	314	293	99.6
HC-C	463	294	63	292	270	99.5
HC-S	504	314	62	313	273	99.4

The galvanostatic charge/discharge curves were carefully analyzed in more detail to provide a deeper understanding of Na insertion in the hard carbons (Fig. 8a–c). The curves have two main regions, one located at a high voltage between 3.0 V and 0.1 V, known as the sloping region, and another one situated in the low potential region (below 0.1 V), called the plateau region.

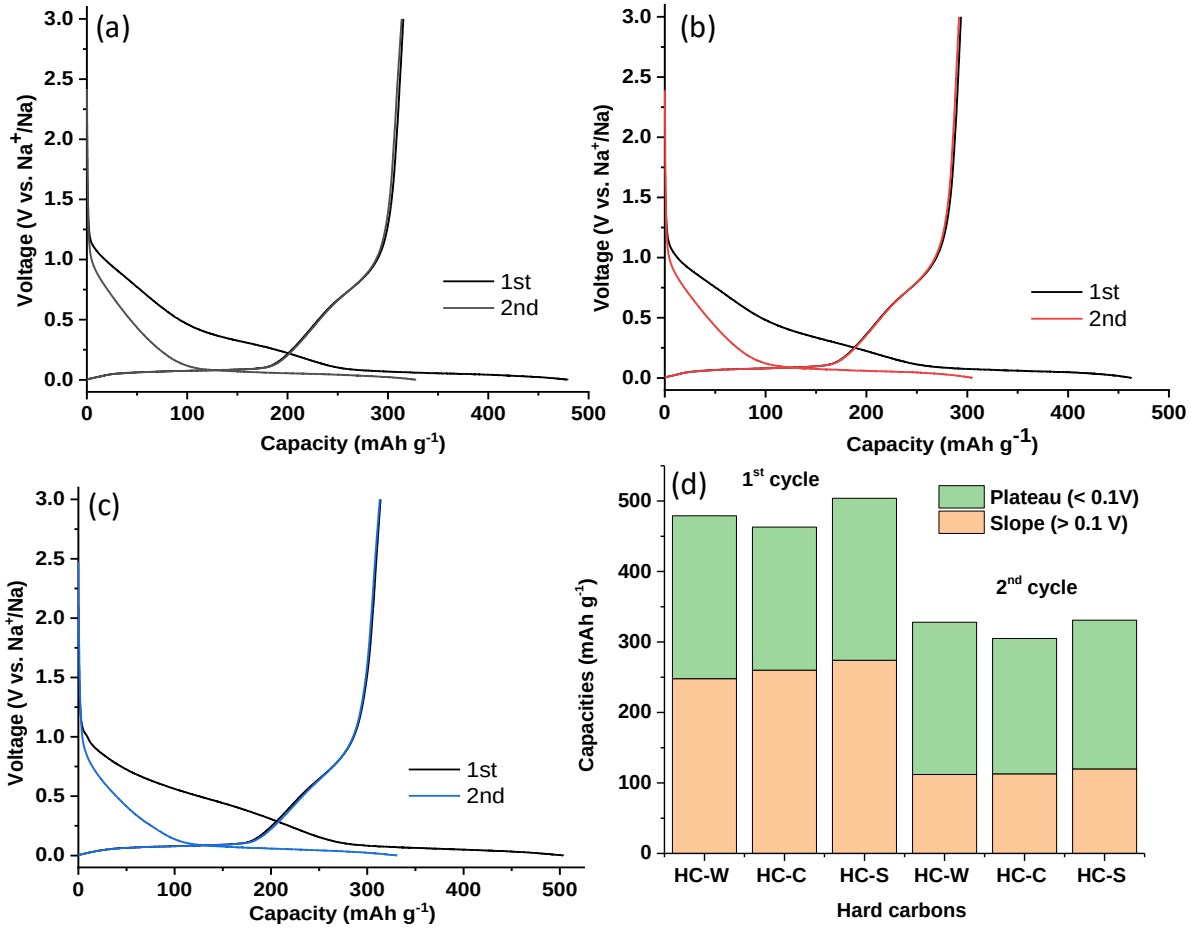

Fig. 8. *1st and 2nd galvanostatic charge/discharge curves of hard carbons (a) HC-W, (b) HC-C, and (c) HC-S and the repartition of the capacity in the sloping and the plateau regions for the first and second charge/discharge cycles (d).*

The insertion of Na in these two regions has been extensively studied; however, their attribution to a certain mechanism is still a highly discussed and controversial subject in the literature, as recently reviewed elsewhere [9, 41]. The first mechanism of Na insertion in HCs was proposed by Stevens and Dahn [4] who assigned the high-voltage sloping region to the intercalation of Na in the HC pseudo-graphitic domains, while the low-voltage plateau region was associated with the adsorption of Na in the nanovoids (nanopores). Such a mechanism is still sustained today by a part of the community [9, 41] whereas since the 2010s, new insights into this topic suggest a rather opposite mechanism, i.e., the adsorption of Na into the pores in the sloping region and intercalation of Na between graphene layers in the plateau region. Moreover, the mechanism of these two sloping regions was revealed to be more complex due to the contribution of other carbon properties to the storage mechanism. Active sites (graphene edge

defects) and functional groups (heteroatoms) were identified to contribute to Na insertion in the sloping region [7, 8, 10] while closed pores adsorb Na in the plateau region [38, 50].

In the first cycle, the repartition of capacity is rather equivalent between the sloping and plateau regions (Fig. 7d), with slightly higher values for the sloping region. Among the materials, HC-W has the smallest sloping capacity (248 mAh g^{-1}; 270 mAh g^{-1} for HC-C and 260 mAh g^{-1} for HC-S). In the second cycle, the contribution from the sloping region was twice as small (112 to 120 mAh g^{-1}) as in the first cycle, suggesting that significant irreversible Na-insertion occurred in this region. Considering the recent mechanisms mentioned above, the insertion of Na in this region is governed by the interactions of Na with the defective graphene sheets and functional groups and the adsorption in the porosity. For instance, HC-W, which had the smallest specific surface area and number of functional groups and impurities, possessed the lowest sloping capacity in the 1st cycle.

Regarding the plateau region, which is linked to the insertion of Na between the pseudo-graphitic domains, the capacity values vary only slightly between the first and second discharge/charge cycles. The highest capacity was observed for HC-W (216 mAh g^{-1}), which can be explained by the better organized structure and the higher carbon active phase in the material. In contrast, the lowest recorded capacity was that of HC-C, which can be associated with its structure containing large graphitic domains with limited d_{002} space for Na intercalation, as revealed using HRTEM and Raman spectroscopy, and indirectly to its high content of inorganic impurities (Table 2), reducing the amount of active carbon in the material.

To provide a deeper understanding of the Na storage mechanism, cyclic voltammetry (CV) and Raman spectroscopy were performed on the HC-W material. The CV analyses recorded at scan rates between 0.1 mV s^{-1} and 1.0 mV s^{-1} (Fig. 9a) provided valuable indications about the electrochemical reaction mechanisms. The power-law ($I = aV^b$) [51] describes the relationship between the peak current (I) and the scan rate (V), discriminating between the two different contributions, i.e., capacitive reactions, which are governed by surface adsorption (when b = 1), and diffusive reactions, which are more linked to the insertion/extraction of Na between the graphitic layers (when b = 0.5). The b value can be assessed by determining the slope of the linear fit of log (I) *vs.* log (V), as shown in Fig. 9(b). The intense anodic peak visible in the low voltage region (~0.1 V *vs.* Na/Na^+) was considered here and b was found to be 0.67. This indicates both capacitive and diffusive mechanisms controlled by the surface and insertion

reactions of Na within the carbon framework. The quantitative repartition of capacitive and diffusive contributions to the overall storage mechanism was determined according to the equations described elsewhere [52, 53] and depicted in Fig. 9(c) for all scan rates. We can see that the capacitive contribution is predominant, and it tended to increase from ~68.7% to 87.0% when the sweep rate increased from 0.2 mV s^{-1} to 1.0 mV s^{-1}, which is in line with other studies [53, 54]. Therefore, these CV results support a mechanism of "adsorption-intercalation," which is in agreement with several recent reports [8, 53-55].

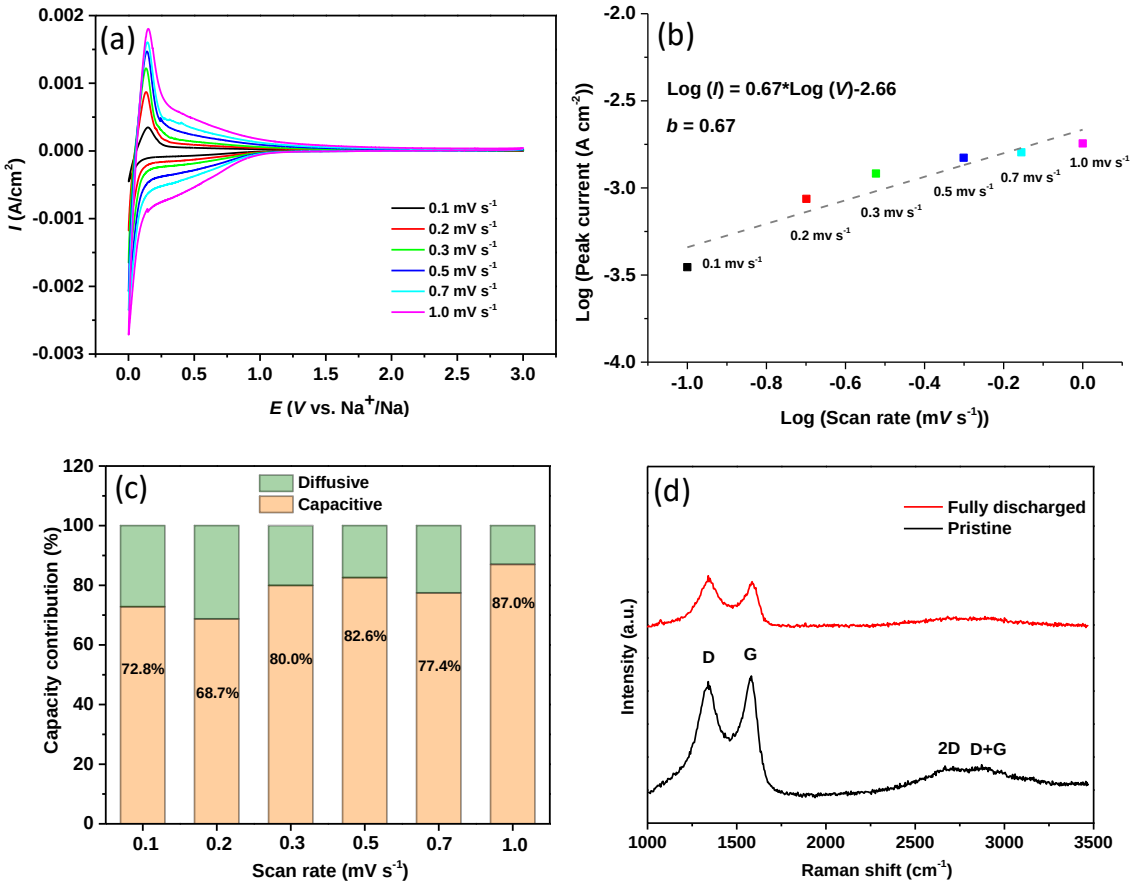

Fig. 9. *(a) Cyclic voltammograms at different scan rates (0.1–1.0 mV s^{-1}) between 0.01 V and 3.0 V vs. Na^+/Na for HC-W material in half-cells, (b) the correlation of peak current with scan rate at low potential (~0.1 V vs. Na/Na^+), (c) repartition of capacity between diffusive and capacitive components for different scan rates (0.1–1.0 mV/s) and (d) ex-situ Raman spectra of a pristine and fully discharged HC-W electrode (25 mA g^{-1} current rate).*

Ex-situ Raman spectroscopy was employed to obtain more knowledge about Na insertion into hard carbon. The HC-W was used as the reference material and *ex situ* Raman spectra of the pristine and fully discharged electrodes are shown in Fig. 9(d). Comparing these two spectra,

one can see that the positions of the D and G bands remain rather unchanged, while their intensity significantly decreases upon discharge. The second-order bands (2D and D+G) are no longer visible after discharge.

Different behaviors of the D and G bands have been reported for hard carbon upon sodiation during *in-situ* Raman spectroscopy, i.e., no shift of D and G bands, as in our work [56, 57]; shift of only the G band [53, 58, 59]; and even a shift of both D and G bands [60]. The G band shift is reported to occur mainly in the high potential sloping region, whereas its position remains constant in the low voltage plateau region [53, 58, 59]. This observation leads authors to consider that the red shift of the G band is related to the intercalation of Na into the graphitic domains. However, even if the D band maintained the same position, its intensity diminished with the sodiation process, thus suggesting the adsorption of Na^+ on the defective sites of pseudo-graphitic and disordered domains. It is worth mentioning that the Raman results discussed above were usually obtained using a single hard carbon material whose properties are distinct from one paper to another. For instance, carbons possessing high surface area (up to 1500 $m^2 g^{-1}$), very low interlayer space close to graphite (< 3.4°), or high amount of defects and heteroatoms [53, 58-60] were used, which are somehow particularly complex hard carbons, making it difficult to understand the observed results and their transposition to "typical" hard carbon (possessing low surface area and large interlayer space). In the case of the latter, it is worth mentioning that the G band shift could not be observed. The analogy of Na insertion into hard carbon with Li insertion into graphite is usually employed for Raman data interpretation; however, this parallel has its own limitations considering the significantly different structure of hard carbon (large D and G bands) and the fact that stable sodiated intercalation compounds are difficult to occur. Therefore, in-depth systematic studies are required to fully understand the Na storage mechanism based on this technique.

In the light of these observation, considering the absence of the G peak shift but the tendency of the D and G peaks to decrease upon sodiation, the Na-storage mechanism seems to be more governed by the adsorption phenomena. This result is consistent with the CV observation, where a predominant capacitive contribution was observed. However, the intercalation of Na in hard carbon the cannot be excluded either.

To present a complete picture of the material performance, in addition to reversible and irreversible capacity, another important characteristic of hard carbons is their capacity

maintenance upon long-term cycling. Fig 10(a) illustrates the capacity retention comparison for all hard carbon negative electrodes when cycled against metallic Na in coin cells at a rate of 50 mA h^{-1}. It can be seen that all the materials exhibit a rather stable evolution of capacity over 100 cycles, with only very little capacity fading. Thus, the capacity varies for HC-W, HC-C, and HC-S from 314, 292, and 313 in the 2nd cycle to 293, 270, and 273 in the 100th cycle, representing a capacity retention of 93%, 92%, and 87%, respectively.

Therefore, high capacity is maintained particularly for HC-W materials, which already possesses low specific surface area, low amount of oxygen groups, and impurities in their structure. For the other two materials, HC-C and HC-S, similar capacities were observed, with the former exhibiting better capacity retention. Both materials contained higher amounts of oxygen than HC-W. In particular, HC-S had some graphitized zones with lower d_{002} space in its structure that may limit the Na-insertion [6] and higher inorganic impurities identified to affect the long-term cycle stability [12].

Comparing the results obtained herein to those reported in other literature on HCs composed of biomass materials (Table 4), it can be seen that the current results are similar or even better if one considers that the fewer higher values observed in the table are recorded either for lower current rates or for a shorter number of cycles. For example, cellulose could deliver a capacity of 325 mAh g^{-1} after 170 cycles but at a low current rate (20 mA g^{-1}) [8]. Similar performance was reported for an argan shell-derived HC (300 mAh g^{-1} after 100 cycles) for low current rate regimes (25 mA g^{-1}) [22]. Finally, hard carbon issued from lotus seed pods showed a similar capacity to our best HC-W carbon (295 mAh g^{-1} at 50 mA·g^{-1} after 200 cycles); however, in this case, the iCE is much smaller (50 vs. 66 for HC-W), probably due to its higher specific surface area (141 *vs.* 6 m^2 g^{-1} for HC-W) [61].

To demonstrate the potential application of the materials, full cells were assembled. A $Na_3V_2(PO_4)_2F_3$ (NVPF) cathode was coupled with a HC-W hard carbon anode. The discharge curves (Fig. 10 c) exhibited a plateau at approximately 4.1 V and a sloping region below 3.5 V, giving an accumulative capacity of 96.7 mAh/(g cathode). Considering the average potential of 3.84 V, it delivered an attractive energy density of 279 Wh/kg (based on the mass of cathode and anode active materials). A slow degradation of capacity over cycling (Fig. 10d) was observed because of the incompatibility between the glyme-based electrolyte and hard carbon

in the full cell, which requires further optimization through the development of effective electrolyte additives [62].

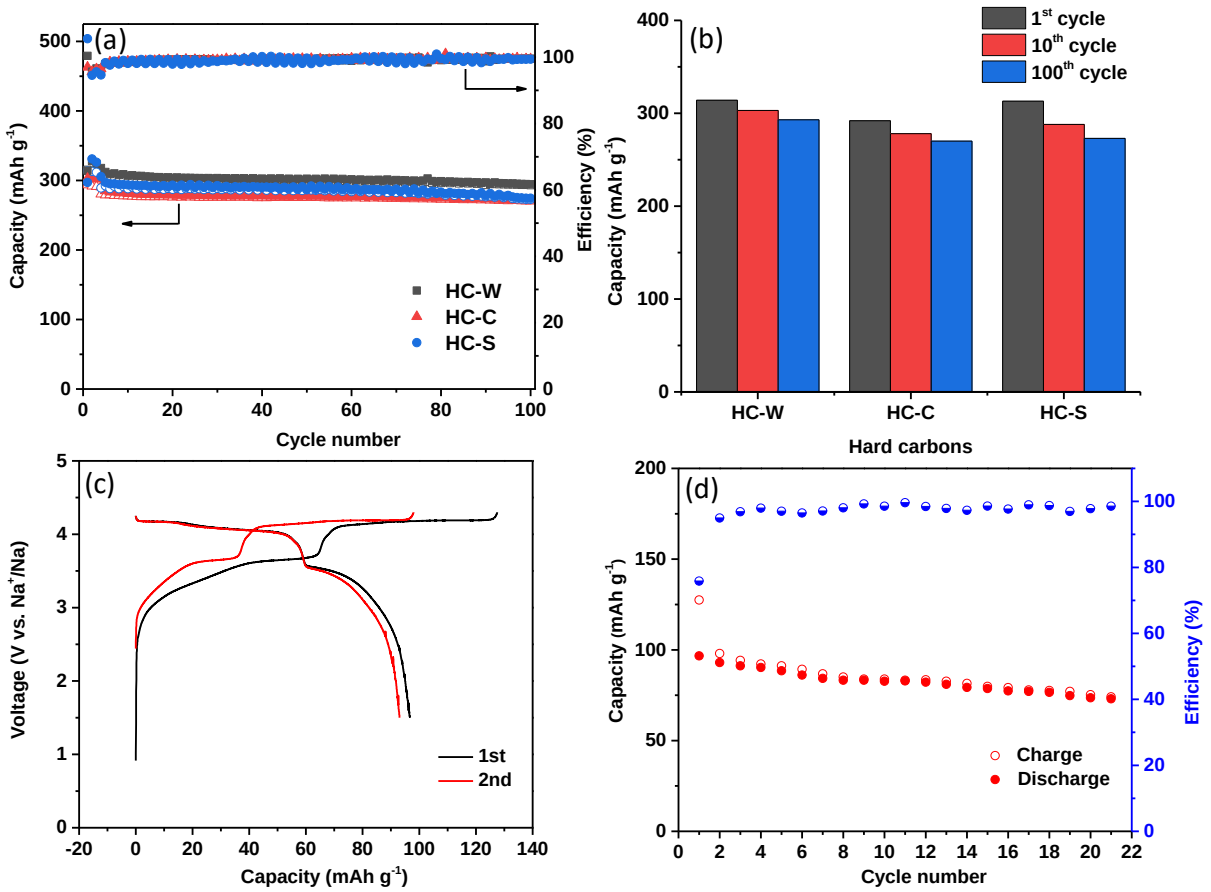

Fig. 10. *(a) Evolution of HCs capacity vs. cycle number along with the coulombic efficiency and (b) capacity vs. selected number of cycles in half-cells, (c) galvanostatic capacity-voltage profiles of the full cell (HC-W // NVPF) during the 1st and 2nd cycles and (d) specific capacity and efficiency evolution vs. cycle number.*

In summary, the results obtained herein demonstrate the possibility of using naturally abundant and available precursors to obtain hard carbon with low surface area and high potential for Na-ion battery applications. Nevertheless, the interface between the carbon and the electrolyte can be further improved to achieve better coulombic efficiency in the first cycle. Some approaches could be the reduction of oxygen functional groups/impurities and the optimization of electrolyte type, electrode formulation, and electrochemical testing conditions, which might reduce undesired irreversible reactions.

Table 4. *Literature performances of biomass waste hard carbons as anodes in Na-ion batteries*.*

Precursor	TT (°C)	S_{BET} (m^2 g^{-1})	d_{002} (Å)	iCE (%)	Cycle ability (mAh· g^{-1})	Electrolyte	Refs.
Cellulose	1300	117	3.77	-	325 at 20 mA g^{-1} after 170 cycles	1 M $NaClO_4$:EC/DEC (1:1 +5 wt% FEC)	[8]
Lignin	1200	10	3.67	79	270 at 37 mA·g^{-1} after 50 cycles	1 M $NaClO_4$:EC/DMC	[13]
Pine	1400	3.0	3.75	83	310 at 37 mA·g^{-1} after 50 cycles	1 M $NaClO_4$:EC/DMC (1:1 +1.5 wt% FEC)	[24]
Argan shells	1300	2.6	3.88	84	300 at 25 mA g^{-1} after 100 cycles	1 M $NaPF_6$:EC/DEC	[22]
Mangosteen shells	1300	82	3.71	74	275 at 20 mA g^{-1} after 100 cycles	1 M $NaClO_4$:EC/PC	[21]
Peat Moss	1400	92	3.83	58	294 at 50 mA·g^{-1} after 10 cycles	1 M $NaClO_4$:EC/DEC	[63]
Lotus Seedpod	1200	141	3.86	50	295 at 50 mA·g^{-1} after 200 cycles	1 M $NaClO_4$:PC (+2 vol% FEC)	[61]
Corn cob	1300	3.7	3.98	86	275 at 60 mA·g^{-1} after 100 cycles	0.6 M $NaPF_6$:EC/DMC	[40]
Walnut	1200	19	3.70	-	254 at 50 mA·g^{-1} after 5 cycles	1 M $NaClO_4$:EC/DMC (1:1 +5 wt% FEC)	[46]
Walnut	1300	6	3.70	66	293 at 50 mA·g^{-1} after 100 cycles	1 M $NaPF_6$-dyglyme	Here

Coconut	1300	**7**	3.75	63	270 at 50 $mA \cdot g^{-1}$ after 100 cycles	1 M $NaPF_6$-dyglyme	Here
Silk	1300	10	3.68	62	273 at 50 $mA \cdot g^{-1}$ after 100 cycles	1 M $NaPF_6$-dyglyme	Here

*EC–ethylene carbonate, DEC–diethyl carbonate; DMC–dimethyl carbonate; PC–propylene carbonate; FEC–fluoroethylene carbonate.

4. Conclusions

Three biomass wastes (walnut shells, coconut shells, and corn silk) were investigated in this work as potential sources to produce hard carbon anodes for Na-ion batteries. Their pyrolysis at 1300 °C followed by acid washing to remove inorganic impurities led to hard carbon materials with low and similar surface areas (< 10 m^2 g^{-1}), which are beneficial for this application. The structure determined using several complementary techniques indicates a higher degree of disorder for coconut shell HC, while for corn silk HC, a mixture of disordered carbon and localized graphitized structure was observed. The latter was associated more likely with Si and/or K metal catalytic *in-situ* graphitization during the pyrolysis process. The surface chemistry of the materials revealed different types of oxygen functional groups, and the coconut shell and corn silk HCs possessed a higher amount of oxygen than the walnut HC. The partial bonding of O to C and the inorganic impurities triggers evidently lower amounts of active carbon in the case of the former HCs compared to the latter. The HCs exhibited good electrochemical performances in Na-half cells, with high reversible capacity varying between 294 and 315 mAh g^{-1} at 50 mA g^{-1} current rate and good retention capacity, i.e., 87% to 93% after 100 charge/discharge cycles. The best reversible capacity was achieved for walnut HC *via* an "adsorption-intercalation" mechanism. This could be associated with the optimal interlayer space and the presence of defective graphene layers. The low surface area and the low amount of inorganic impurities also led to the highest initial coulombic efficiency and the best capacity retention. Full-cell assembled with walnut HC revealed a high capacity of 96.7 mAh/($g_{cathode}$) and an attractive energy density of 279 Wh/kg. The present results are slightly better than those of previous reports on biomass-derived HCs and demonstrate the potential of renewable and highly available precursors for the fabrication of anode materials for novel Na-ion battery implementation.

Declaration of Conflicts of Interest

The authors declare no competing interests.

Acknowledgments

This work is financially supported by the European Union's Horizon 2020 Program (project NAIADES, call: LCE10-2014, Contract no. 646433). The authors thank Dr. Jean-Marc Le Meins, Dr. Samar Hajjar, and Dr. Loic Vidal for their support with the XRD, XPS, and TEM analyses *via* the IS2M technical platform.

References

[1] B. Dunn, H. Kamath, J.M. Tarascon, Science, 334 (2011) 928-935.
[2] N. Yabuuchi, K. Kubota, M. Dahbi, S. Komaba, Chemical Reviews, 114 (2014) 11636-11682.
[3] Y. Liu, B.V. Merinov, W.A. Goddard, Proceedings of the National Academy of Sciences, 113 (2016) 3735-3739.
[4] D.A. Stevens, J.R. Dahn, Journal of The Electrochemical Society, 148 (2001) A803-A811.
[5] C. Bommier, T.W. Surta, M. Dolgos, X. Ji, Nano Letters, 15 (2015) 5888-5892.
[6] Y. Cao, L. Xiao, M.L. Sushko, W. Wang, B. Schwenzer, J. Xiao, Z. Nie, L.V. Saraf, Z. Yang, J. Liu, Nano Letters, 12 (2012) 3783-3787.
[7] C. Matei Ghimbeu, J. Górka, V. Simone, L. Simonin, S. Martinet, C. Vix-Guterl, Nano Energy, 44 (2018) 327-335.
[8] S. Qiu, L. Xiao, M.L. Sushko, K.S. Han, Y. Shao, M. Yan, X. Liang, L. Mai, J. Feng, Y. Cao, X. Ai, H. Yang, J. Liu, Advanced Energy Materials, 7 (2017) 1700403.
[9] D. Saurel, B. Orayech, B. Xiao, D. Carriazo, X. Li, T. Rojo, Advanced Energy Materials, 8 (2018) 1703268.
[10] B. Zhang, C.M. Ghimbeu, C. Laberty, C. Vix‐Guterl, J.-M. Tarascon, Advanced Energy Materials, 6 (2016) 1501588.
[11] C. Bommier, W. Luo, W.-Y. Gao, A. Greaney, S. Ma, X. Ji, Carbon, 76 (2014) 165-174.
[12] J.M. Conder, C. Vaulot, C. Marino, C. Villevieille, C.M. Ghimbeu, ACS Applied Energy Materials, 2 (2019) 4841–4852.
[13] C. Matei Ghimbeu, B. Zhang, A. Martinez de Yuso, B. Rety, J.-M. Tarascon, Carbon, 153 (2019) 634-647.
[14] V. Simone, A. Boulineau, A. de Geyer, D. Rouchon, L. Simonin, S. Martinet, J Energy Chem, 25 (2016) 761-768.
[15] A. Beda, P.-L. Taberna, P. Simon, C. Matei Ghimbeu, Carbon, 139 (2018) 248-257.
[16] Y. Li, L. Mu, Y.-S. Hu, H. Li, L. Chen, X. Huang, Energy Storage Materials, 2 (2016) 139-145.
[17] P.-Y. Zhao, B.-J. Yu, S. Sun, Y. Guo, Z.-Z. Chang, Q. Li, C.-Y. Wang, Electrochimica Acta, 232 (2017) 348-356.
[18] J. Górka, C. Vix-Guterl, C. Matei Ghimbeu, C, 2 (2016) 24.
[19] K. Kim, D.G. Lim, C.W. Han, S. Osswald, V. Ortalan, J.P. Youngblood, V.G. Pol, ACS Sustainable Chemistry & Engineering, 5 (2017) 8720-8728.

[20] E.M. Lotfabad, J. Ding, K. Cui, A. Kohandehghan, W.P. Kalisvaart, M. Hazelton, D. Mitlin, ACS Nano, 8 (2014) 7115-7129.
[21] K. Wang, Y. Jin, S. Sun, Y. Huang, J. Peng, J. Luo, Q. Zhang, Y. Qiu, C. Fang, J. Han, ACS Omega, 2 (2017) 1687-1695.
[22] M. Dahbi, M. Kiso, K. Kubota, T. Horiba, T. Chafik, K. Hida, T. Matsuyama, S. Komaba, Journal of Materials Chemistry A, 5 (2017) 9917-9928.
[23] Q. Jiang, Z.H. Zhang, S.Y. Yin, Z.P. Guo, S.Q. Wang, C.Q. Feng, Applied Surface Science, 379 (2016) 73-82.
[24] C.d.M. Saavedra Rios, V. Simone, L. Simonin, S. Martinet, C. Dupont, Biomass and Bioenergy, 117 (2018) 32-37.
[25] S.-D. Xu, Y. Zhao, S. Liu, X. Ren, L. Chen, W. Shi, X. Wang, D. Zhang, Journal of Materials Science, 53 (2018) 12334-12351.
[26] N. Zhang, Q. Liu, W.L. Chen, M. Wan, X.C. Li, L.L. Wang, L.H. Xue, W.X. Zhang, Journal of Power Sources, 378 (2018) 331-337.
[27] X.M. Zhu, X.Y. Jiang, X.L. Liu, L.F. Xiao, Y.L. Cao, Green Energy & Environment, 2 (2017) 310-315.
[28] A. Gomez-Martin, J. Martinez-Fernandez, M. Ruttert, M. Winter, T. Placke, J. Ramirez-Rico, Chemistry of Materials, 31 (2019) 7288-7299.
[29] in, pp. https://www.statista.com/statistics/577497/world-coconut-production/.
[30] in, pp. https://www.bioenergyconsult.com/coconut-biomass/.
[31] N. Arena, J. Lee, R. Clift, Journal of Cleaner Production, 125 (2016) 68-77.
[32] A.O. Ogah, J.N. Afiukwa, Journal of Reinforced Plastics and Composites, 33 (2014) 37-46.
[33] L.R. Radovic, CRC Press, 2019.
[34] K. Acikalin, Journal of Thermal Analysis and Calorimetry, 105 (2011) 145-150.
[35] Y.R. Fan, G.D. Fowler, C. Norris, Industrial & Engineering Chemistry Research, 56 (2017) 4779-4791.
[36] T. Rout, D. Pradhan, R.K. Singh, N. Kumari, Journal of Environmental Chemical Engineering, (2016) 3696-3705.
[37] E. Irisarri, N. Amini, S. Tennison, C.M. Ghimbeu, J. Gorka, C. Vix-Guterl, A. Ponrouch, M.R. Palacin, Journal of The Electrochemical Society, 165 (2018) A4058-A4066.
[38] Y.Q. Li, Y.X. Lu, Q.S. Meng, A.C.S. Jensen, Q.Q. Zhang, Q.H. Zhang, Y.X. Tong, Y.R. Qi, L. Gu, M.M. Titirici, Y.S. Hu, Advanced Energy Materials, 9 (2019) 1902852.
[39] M.K. Rybarczyk, Y.M. Li, M. Qiao, Y.S. Hu, M.M. Titirici, M. Lieder, Journal of Energy Chemistry, 29 (2019) 17-22.
[40] P. Liu, Y.M. Li, Y.S. Hu, H. Li, L.Q. Chen, X.J. Huang, Journal of Materials Chemistry A, 4 (2016) 13046-13052.
[41] H. Hou, X. Qiu, W. Wei, Y. Zhang, X. Ji, Advanced Energy Materials, 7 (2017) 1602898.
[42] J. Hoekstra, A. Beale, F. Soulimani, M. Versluijs-Helder, J. Geus, L. Jenneskens, J Phys Chem C, 119 (2015) 10653-10661.
[43] E.R. Buiel, A.E. George, J.R. Dahn, Carbon, 37 (1999) 1399-1407.
[44] J. Fondard, E. Irisarri, C. Courreges, M.R. Palacin, A. Ponrouch, R. Dedryvere, Journal of the Electrochemical Society, 167 (2020) 070526.
[45] E. Peled, S. Menkin, Journal of The Electrochemical Society, 164 (2017) A1703-A1719.
[46] M. Wahid, Y. Gawli, D. Puthusseri, A. Kumar, M.V. Shelke, S. Ogale, Acs Omega, 2 (2017) 3601-3609.
[47] M. Wahid, D. Puthusseri, Y. Gawli, N. Sharma, S. Ogale, ChemSusChem, 11 (2018) 506-526.

[48] C. del Mar Saavedra Rios, L. Simonin, A. de Geyer, C. Matei Ghimbeu, C. Dupont, Energies, 13(14) (2020) 3513.
[49] J. Conder, C. Villevieille, Chemical Communications, 55 (2019) 1275-1278.
[50] Y. Morikawa, S. Nishimura, R. Hashimoto, M. Ohnuma, A. Yamada, Advanced Energy Materials, 10 (2020) 1903176.
[51] J. Wang, J. Polleux, J. Lim, B. Dunn, Journal of Physical Chemistry C, 111 (2007) 14925-14931.
[52] W.W. Hong, Y. Zhang, L. Yang, Y. Tian, P. Ge, J.G. Hu, W.F. Wei, G.Q. Zou, H.S. Hou, X.B. Ji, Nano Energy, 65 (2019) 104038.
[53] X.W. Zhong, Y.Z. Li, L.Z. Zhang, J. Tang, X.N. Li, C. Liu, M.M. Shao, Z.G. Lu, H. Pan, B.M. Xu, Acs Applied Materials & Interfaces, 11 (2019) 2970-2977.
[54] Q.Z. Jin, K.L. Wang, P.Y. Feng, Z.C. Zhang, S.J. Cheng, K. Jiang, Energy Storage Materials, 27 (2020) 43-50.
[55] N. Sun, Z. Guan, Y. Liu, Y. Cao, Q. Zhu, H. Liu, Z. Wang, P. Zhang, B. Xu, Advanced Energy Materials, 9 (2019) 1901351.
[56] X. Lin, X. Du, P.S. Tsui, J.-Q. Huang, H. Tan, B. Zhang, Electrochimica Acta, 316 (2019) 60-68.
[57] X.Y. Lin, Y.Z. Liu, H. Tan, B. Zhang, Carbon, 157 (2020) 316-323.
[58] S. Huang, Z. Li, B. Wang, J. Zhang, Z. Peng, R. Qi, J. Wang, Y. Zhao, Advanced Functional Materials, 28 (2018) 1706294.
[59] M.A. Reddy, M. Helen, A. Gross, M. Fichtner, H. Euchner, Acs Energy Letters, 3 (2018) 2851-2857.
[60] Z.J. Zheng, Q. Su, Q. Zhang, H. Ye, Z.B. Wang, Journal of Materials Science, 53 (2018) 12421-12431.
[61] F. Wu, M.H. Zhang, Y. Bai, X.R. Wang, R.Q. Dong, C. Wu, Acs Applied Materials & Interfaces, 11 (2019) 12554-12561.
[62] K. Westman, R. Dugas, P. Jankowski, W. Wieczorek, G. Gachot, M. Morcrette, E. Irisarri, A. Ponrouch, M.R. Palacin, J.M. Tarascon, P. Johansson, Acs Applied Energy Materials, 1 (2018) 2671-2680.
[63] J. Ding, H. Wang, Z. Li, A. Kohandehghan, K. Cui, Z. Xu, B. Zahiri, X. Tan, E.M. Lotfabad, B.C. Olsen, D. Mitlin, ACS Nano, 7 (2013) 11004-11015.